

TIME-AND-SPATIALLY ADAPTING SIMULATIONS FOR EFFICIENT DYNAMIC STALL PREDICTIONS

Marilyn J. Smith
Professor
Georgia Tech

Rohit Jain
Aerospace Engineer
US Army - AFDD

Amanda Grubb
M.S. Candidate
Georgia Tech

Kevin Jacobson
Ph.D. Candidate
Georgia Tech

Georgia Institute of Technology
School of Aerospace Engineering
Atlanta, Georgia, 30332, USA

US Army Aviation Development Directorate - AFDD
Aviation & Missile Research, Development & Engineering Center
Research, Development and Engineering Command (RDECOM)
Moffett Field, California, 94035, USA

ABSTRACT

The ability to accurately and efficiently predict the occurrence and severity of dynamic stall remains a major roadblock in the design and analysis of conventional rotors as well as new concepts for future vertical lift. Several approaches to reduce the cost of these dynamic stall simulations for airfoils and finite wings are investigated. Temporal error controllers, variable time step sizes, and feature-based near-body mesh adaptation are evaluated for their ability to more cost-effectively predict dynamic stall on three different configurations. A fourth-order temporal controller has been observed to provide a balanced cost-accuracy ratio, as a maximum of three to four orders of magnitude convergence of the Newton subiterations is obtained during much of the dynamic stall cycle. Larger time steps can be applied, in particular during the attached upstroke portion of the dynamic stall cycle with fourth-order temporal convergence. Mesh reductions via a feature-based two-level adaptation provided a 50% reduction in computational costs with comparable accuracy to a fixed, refined mesh size. Additional refinements may be warranted just after the dynamic stall onset to capture the complex flow field.

NOTATION

a_∞	Free-stream speed of sound [m/s]
AR	Blade aspect ratio, b^2/S
c	Blade chord length [m]
d	Projected diameter of the airfoil [m]
k	Reduced frequency, $\omega c/2U_\infty$
M_∞	Free-stream Mach number, U_∞/a_∞
Q	Flow variable
R	Wing span [m]
Re	Reynold number, $U_\infty c/\nu_\infty$
U_∞	free-stream velocity [m/s]
α	Angle of attack [rad]
ω	Blade angular velocity [rad/s]

1 INTRODUCTION

Goals for future vertical lift (FVL) concepts include rotors that no longer encounter dynamic stall, a phenomenon that has limited the forward flight speed of helicopters. The ability to computationally predict the

onset of dynamic stall, as well as its severity, is necessary to design these new rotor blades. Furthermore, the ability to accurately predict dynamic stall on current vehicles^[1] is also required as their mission roles change and expand with new technology such as more powerful engines.

The study of dynamic stall has encompassed several decades. Significant progress in experimental analysis was made in the since the 1980s by a number of researchers, including but not limited to McCroskey^[2,3], Carr^[4], Lorber^[5,6] and Piziali^[7]. Recent advances in Particle Image Velocimetry (PIV) and unsteady pressure sensors provide unsteady flow field and performance quantities together to advance knowledge in dynamic stall physics for a variety of configurations and operating conditions^[8-11].

Many numerical studies have also been undertaken, but progress was limited until the past decade. The advancement of high performance computing on massively parallel processors provides the ability to simulate these processes with millions of degrees of freedom necessary to model these complex phenomena. These large resources have permitted rotorcraft researchers^[12-16] to analyze grids, spatial convergence, and turbulence models for two-dimensional airfoils. Initial studies focused primarily

Presented at the 41st European Rotorcraft Forum, Munich, Germany, September 1-4, 2015.

This material is declared a work of the U.S. Government and is not subject to copyright protection in the United States. DISTRIBUTION STATEMENT A. Approved for public release; distribution is unlimited.

on grid dependence for static stall with several turbulence models [12,13], as an initial step prior to dynamic stall. Costes et al. [14] revealed non-physical flow phenomena (chord-wise oscillations in the suction peaks and skin friction profiles resembling transition) due to numerical errors even though the solutions appeared to be converged.

Subsequent dynamic stall evaluations [15,17,18] identified boundary layer reattachment as the feature most sensitive to spatial and temporal resolution. Based on visual inspection of stall onset and flow reattachment, they recommended 360,000 time steps/cycle \times subiterations for convergence. Klein, Richter, and Altmikus [16] reaffirmed the sensitivity of reattachment to time step size and recommended 1000 to 2000 time steps per cycle with 100 subiterations for temporal convergence. Liggett and Smith [18] conducted a detailed temporal analysis, identifying a cutoff point below which the simulations remained first order even with the use of Newton subiterations. They also identified an approach to estimate the accuracy of a mesh for time independence. Burgess and Jain [19] further explored and confirmed the role of subiterations and convergence for dynamic stall.

The lack of fidelity in turbulence and transition closures have been identified as primary culprits in the lack of success in prior dynamic stall simulations. Unsteady Reynolds-averaged Navier-Stokes (URANS) turbulence models are statistical closures. Two-equation models have been shown by numerous researchers to be superior to one-equation models, the latest of these by Kaufmann et al. [20]. Improved correlations with experiment are obtained when the URANS models are replaced with delayed detached eddy simulation (DDES) or hybrid URANS-Large Eddy Simulation (LES) turbulence closures [18,21]. Transition remains elusive and dependent on the configuration and operational conditions, with some researchers reporting improved correlations with experiment [20] when transition is applied, while others do not [22].

In all of these recent dynamic stall simulation efforts, researchers agree that an accurate simulation of dynamic stall requires very fine meshes and small time step sizes. The meshes are typically much more refined than industry-level rotor meshes, up to an order of magnitude. The dense mesh spacing required in two-dimensions can be coarsened when three-dimensional relief effects associated with separated flows are included. However, the temporal requirements translate to one to two orders of magnitude smaller physical time steps than are usually applied to rotors, as well as an order of magnitude increase in the number of Newton subiterations in dual time stepping schemes.

These spatial and temporal requirements are a bottleneck in achieving accurate rotor simulations that

include dynamic stall. Significant reduction in the computational cost, while maintaining the accuracy of the aerodynamic performance predictions are sought. This effort investigates several different approaches that may provide increased speed and memory reduction through the application of temporal and spatial adaptation and control.

2 NUMERICAL MODEL

The numerical simulations were conducted using OVERFLOW 2.2, a structured solver with Chimera overset grid capabilities [23]. For the computations in this effort, spatial terms were discretized using a fourth-order central difference algorithm incorporating a diagonalized Beam-Warming scalar pentadiagonal scheme. Second-order temporal integration was achieved by applying Newton subiterations to a first-order implicit Euler scheme. Artificial dissipation was included using the spectral-based dissipation scheme.

The second-order temporal discretization discussed above has been implemented in a large number of flow solvers, including FUN3D [24] and OVERFLOW [25]. The user must select the number of subiterations that is applied at each physical time step. A large number of pseudo time steps will ensure proper temporal convergence, but will also be prohibitive in terms of CPU cost. It is therefore of the utmost importance to develop a criterion that will recover the full temporal accuracy of the scheme while maintaining a reasonable cost. The temporal error introduced by the backward difference formulation (BDF) schemes can be estimated by examining the residuals obtained with two different levels of approximations of the time derivatives [26]. The time derivative in the Navier-Stokes equations can be written as

$$(1) \left(\frac{\partial \mathbf{Q}}{\partial t} \right)^A = \frac{1}{\Delta t} (\phi_{n+1}^A \mathbf{Q}^{m+1} + \phi_n^A \mathbf{Q}^n + \phi_{n-1}^A \mathbf{Q}^{n-1} + \phi_{n-2}^A \mathbf{Q}^{n-2} + \dots)$$

$$\left(\frac{\partial \mathbf{Q}}{\partial t} \right)^B = \frac{1}{\Delta t} (\phi_{n+1}^B \mathbf{Q}^{m+1} + \phi_n^B \mathbf{Q}^n + \phi_{n-1}^B \mathbf{Q}^{n-1} + \phi_{n-2}^B \mathbf{Q}^{n-2} + \dots)$$

where the superscript A and B represents different BDF schemes (see Table 1). In the actual solver, A will correspond to the main temporal scheme and B to the BDF scheme with the accuracy immediately below (BDF1 for BDF2, BDF2 for BDF2_{opt}, etc.). Subtracting the two time derivatives in Eq. (2), one can estimate the temporal error of the solution from time

level n to $m + 1$:

$$(2) \left(\frac{\partial \mathbf{Q}}{\partial t} \right)^A - \left(\frac{\partial \mathbf{Q}}{\partial t} \right)^B = \frac{1}{\Delta t} [(\phi_{n+1}^A - \phi_{n+1}^B) \mathbf{Q}^{m+1} + (\phi_n^A - \phi_n^B) \mathbf{Q}^n + (\phi_{n-1}^A - \phi_{n-1}^B) \mathbf{Q}^{n-1} + (\phi_{n-2}^A - \phi_{n-2}^B) \mathbf{Q}^{n-2} + \dots]$$

and the temporal error norm is given by

$$(3) E_t = \Delta t \left\| \left(\frac{\partial \mathbf{Q}}{\partial t} \right)^A - \left(\frac{\partial \mathbf{Q}}{\partial t} \right)^B \right\|$$

Most solvers including OVERFLOW apply the L_∞ norm to assess convergence. The subiterations are discontinued, and the next time step initiated when the residuals (algebraic error) descend below a specified fraction of the temporal error norm E_t . A drop of at least one order of magnitude is typically recommended in the literature^[25], but there have been few investigations to date that have quantitatively confirmed this value, in particular for dynamic stall.

3 RESULTS AND DISCUSSION

Three different configurations were evaluated numerically in this study. Two-dimensional computations for the NACA0012 and VR7 (no tab) airfoils to assess and define the analysis before most costly three-dimensional analyses were undertaken. Correlations were made with experimental data from McCroskey^[2] and Kearney^[9], respectively. Three-dimensional computations to confirm the observations and demonstrate the methods were obtained for the OA209 finite wing^[11]. As noted previously in the Introduction of this paper, while the URANS turbulence closures and two-dimensional simulations are not exact, they can provide insight into the behavior of the simulations in three-dimensions, as demonstrated previously by Liggett and Smith^[18] at a lower cost than with advanced turbulence closures.

3.1 Temporal Analysis

In this effort, two types of temporal adaptation are evaluated: a temporal error controller for Newton subiterations and change of the physical time step based on the flow field and/or simulation features. The convergence of the Newton subiterations was measured by taking the L_∞ norm of the right hand side residuals.

First, the influence of controlling residual error during the Newton subiterations were investigated for a NACA0012 airfoil undergoing dynamic stall at a $M_\infty = 0.291$ and a chord-based Reynolds number of $Re_c = 3.76 \times 10^6$. The angle of attack motion was $\alpha =$

$5^\circ \pm 10^\circ * \sin(2\omega t)$ at a reduced frequency of $k = 0.1$. Two-dimensional simulations with the Menter Shear Stress Transport (SST) turbulence model^[27] were performed for 9,000 physical time steps per cycle with 20 Newton subiterations, based on the recommendations of Liggett and Smith^[18]. The NACA 0012 O-grid consisted of 200 points normal to the airfoil and 971 circumferential points, with 20 of those being located along the blunt trailing edge. The stream-wise points were distributed equally over the upper and lower surfaces of the airfoil. The initial cell spacing at the wall was chosen to ensure that $y^+ < 1$ and that at least 35-50 normal cells resolve the boundary layer. The convective and viscous terms were both discretized using fourth-order central differences with TLNS3D dissipation, while time derivatives were discretized using the BDF2_{opt} scheme. The linear system of equations was solved implicitly using the approach of Beam & Warming. The order of magnitude was evaluated for convergence for 1-6 orders of magnitude, which was the maximum that could be reached successfully with these simulation conditions.

Figure 1 illustrates the airfoil performance predicted by these simulations compared with experimental data. As typically observed for URANS two-dimensional simulations, the nonlinear lift is over predicted and dynamic stall occurs two to four degrees higher than experiment. The fourth- and sixth-order error controllers provide the most accurate predictions for all three integrated quantities given the simulation and mesh limitations. In particular, sufficient temporal resolution is necessary to minimize the onset of nonlinear lift and stall, improving the simulation by almost two degrees angle of attack. Fourth- or sixth-order convergence is also necessary to correctly capture the reattachment and linear lift curve slope on the upstroke. Drag and pitching moment upstroke predictions in the linear region is not as sensitive to residual magnitude. The magnitude of the negative pitching moment is not influenced significantly, indicating that mesh refinement or turbulence modeling plays a more key role for this variable.

The order of magnitude convergence that was achieved during the final cycle of the analysis is illustrated in Fig. 2. It is clear from this figure why the fourth- and sixth-order results are so similar; over the portion of the simulation which was not in the linear upstroke, the full number of subiterations were completed before the prescribed order of magnitude convergence was reached. To determine if the solution accuracy could be improved by additional subiterations, the number of Newton subiterations was increased from 40 to 100 for fourth-order convergence. The differences observed between the two simulations lie primarily in the downstroke during separated flow. The initial stall event occurred less than 0.5° earlier, with a reduction of about 0.1 in lift coefficient at

Scheme	ϕ_{n+1}	ϕ_n	ϕ_{n-1}	ϕ_{n-2}
BDF1	1	-1	0	0
BDF2	3/2	-2	1/2	0
BDF3	11/6	-3	3/2	-1/3
BDF2 _{opt}	$3/2 - \phi_{n-2}$	$-2 + 3\phi_{n-2}$	$1/2 - 3\phi_{n-2}$	-0.58/3

Table 1: Coefficients for standard BDF schemes up to third order

the peak. Similar behavior is found for the drag coefficient and pitching moment coefficient. The additional cost-to-accuracy ratio for the simulation should be addressed in three-dimensional simulations.

It is clear that first- and second-order convergence is reached throughout the angle of attack cycle except the initial dynamic stall region in Fig. 2. It is important to note that even when there appears to be coincidental convergence characteristics (e.g., the fourth- and sixth-order curves in Fig. 2), the integrated performance characteristics still include minor differences in the region where the convergence appears to be identical (Fig 1). This implies that the higher convergence obtained in other regions of the dynamic stall region may influence the temporal integration.

The convergence has a distinctive impact on the flow field behavior, as illustrated in Fig. 3 for the non dimensional velocity (U/U_∞) for the first (1OM) and fourth (4OM) order of magnitude residual convergence. As the airfoil approaches 17° , the 4OM flow over the suction side influences a larger area near the leading edge, producing an earlier nonlinear lift rise at 20° . By 22° the 4OM flow field has stalled, while the 1OM flow field is still undergoing some vortex-induced lift. During the next three degrees of angle of attack, the 4OM flow field indicates stronger and more developed flow field features associated with stall. For example, in Fig. 3i (1OM), the development and shedding of the vortex at the trailing edge is clearly slower than at the same time in Fig. 3l (4OM), where it is located about 1/2 chord downstream from the trailing edge and weaker.

While Liggett and Smith^[18] indicated that, in terms of the integrated performance quantities, temporal accuracy could be measured by time steps per cycle \times Newton subiterations, this point is revisited with the temporal error controller. Evaluations of 4,500 (with 40 subiterations) and 18,000 (with 10 subiterations) time steps per cycle were examined. As the number of time steps per cycle increased, airfoil performance improvements were observed with the lower order of magnitude (1OM and 2OM), though they never reached comparable results to the higher order of magnitude results (4OM and 6OM). No change in the predictions of the fourth (4OM) and sixth (6OM) predictions were observed with differing time step size. In all cases, the 6OM required all subiterations and the 4OM required almost all subiterations (Fig. 4). Reduc-

tion in the number of maximum subiterations did not permit the solution to converge sufficiently, resulting in less accurate simulations, similar to results shown by Liggett and Smith^[18].

These results were affirmed by a series simulations performed on the VR7 airfoil without a trailing edge tab. This secondary airfoil configuration was selected to ensure that the observations and results observed for the NACA0012 airfoil were extensible to other airfoils. Similar results were obtained for the VR7 airfoil undergoing dynamic stall at a $M_\infty = 0.2$ and a chord-based Reynolds number of $Re_c = 0.5 \times 10^6$. The angle of attack motion was $\alpha = 10^\circ \pm 10^\circ * \sin(2\omega t)$ for a reduced frequency of $k = 0.13$. Data comparisons were made with experimental data obtained by Kearney and Glezer^[9] at Georgia Tech. Their data was obtained at a lower Mach number ($M_\infty = 0.044$, $Re_c = 0.3 \times 10^6$). To negate the need for low Mach number preconditioning, the Mach number was increased for the OVERFLOW compressible flow solver. While there are some differences in the data, the data trends are consistent. Five and ten thousand time steps per cycle with 40 and 20 subiterations, respectively were analyzed. Between three to four orders of magnitude reduction in the right hand side residuals were obtained, similar to the NACA0012. Lower order of magnitude error controller selections resulted in less accurate solutions. As these results are similar to the NACA0012, they are not depicted.

The results of the simulations for both the NACA0012 and the VR7 airfoils imply that the physical time step size could be increased over the linear range, which may result in a significant savings in computational costs, in addition to the savings by choosing the correct temporal controller. To examine this further, an adaptive time step size for the VR7 case was investigated. A simple adaptation based on the direction of the angle of attack was evaluated. The upstroke was modeled at 5000 time steps per cycle, while the downstroke included 10,000 time steps per cycle. The number of subiterations (20) was kept at the smaller time step size (10,000 time steps per cycle) throughout the simulation. This is based on the results of NACA0012 and VR7 order of magnitude study that indicated that the number of subiterations needed to reach four orders of magnitude reduction were fewer than 20 over this range (Fig. 4). The re-

sults of the simulation are presented in Fig. 5. The simulation results are comparable for all approaches (fixed and adaptive time steps) on the upstroke, as indicated by the coincident lines. The switch to the smaller time step occurred at 20° . By the third iteration, no perceptible change in the integrated forces and moments at the time step was noticeable. Further evaluation of the mass and momentum flux over this change were comparable between the fixed and adaptive time steps, indicating no loss of conservation. On the downstroke, by the third cycle, the integrated quantities are observed to be comparable to the 10,000 time step predictions. The cost of this simulation required approximately 49%-50% less than that of the fixed time step of 10,000 steps/cycle and 20 Newton subiterations.

While this simple time step adaption is sufficient for this case, a more sophisticated adaptive parameter would be required for full rotor simulations. This parameter would preferably identify the onset of dynamic stall, in particular the nonlinear lift just before stall. Based on recent experimental research at Georgia Tech by Kearney and Glezer^[9], one such parameter is the vorticity flux ($u_i\omega$) that shows significant change just before and at the onset of dynamic stall. Further development of a consistent and efficient time adaptive scheme is underway.

3.2 Spatial Adaptation Feasibility Study

A two-dimensional OA209 airfoil was evaluated with the feature-based mesh adaptation features in OVERFLOW 2.2^[28]. The mesh adaptation feature sensor was the undivided difference of the flow field conserved variables, \mathbf{Q} :

$$(4) \quad \max_{i=j,k,l} \left[\frac{0.5(\mathbf{Q}_{i+1} - 2\mathbf{Q}_i + \mathbf{Q}_{i-1})}{\mathbf{Q}_{ref}} \right]^2$$

The dynamic stall was evaluated at a Mach number $M_\infty = 0.31$ with a corresponding Reynolds number per chord of $Re_c = 1.2 \times 10^6$. The airfoil motion of $\alpha = 13^\circ \pm 7^\circ \sin(\omega t)$ at a reduced frequency of $k = 0.05$ has also been evaluated and previously published by ONERA and DLR^[17], as illustrated in Fig. 6. The experimental data (in gray) and CFD results using the Spalart-Allmaras turbulence models indicate discrepancies that are normally observed using URANS turbulence closures in two-dimensional simulations: pitching moment and lift overshoot and phase lags at the onset of the dynamic stall, as well as varying recovery rates. To obtain these results, the simulations required 360,000 combined time steps and subiterations on meshes that ranged from 125,000 (Tau) to 400,000 (elsA) points.

Similar integrated results were obtained with OVERFLOW 2.2 for the Spalart-Allmaras turbulence model for a mesh of 2M points, as observed in Fig. 7. The time stepping was 1080 steps per cycle with 20 Newton subiterations for the Eulerian flow with an additional 4 turbulent subiterations at each Newton subiteration. This result formed the basis for the mesh adaptation study. The mesh was then coarsened to provide a basis of analysis for the mesh adaptation. The initial size of the near body mesh was set to 0.128 M ($417 \times 103 \times 3$) with an off-body Cartesian mesh of approximately 0.1M, as illustrated in Fig. 8.

As the simulation progressed, the airfoil was adapted with two levels of refinement at every ten time steps, as illustrated in Fig. 9. The mesh adaptation with respect to the angle of attack indicates that the mesh refinement is required during the initial vortex shedding that characterizes the nonlinear lift increase just prior to dynamic stall. The maximum mesh refinement occurs during the minimum pitching moment where vorticity is shed and found in the near wake from both the leading and trailing edges (Fig. 10). Interestingly, the mesh refinement is minimal during the reattachment phase, although Liggett and Smith^[18] noted that this was a very sensitive area temporally. This implies that reattachment is likely temporally driven rather than mesh driven, given a sufficient mesh size. The integrated airfoil performance (Fig. 10) indicates that the adaptive mesh can predict comparable results to the larger fixed mesh, confirming that this approach is sufficient. The goal in these computations was not to optimize the mesh adaptation size, but to illustrate that the mesh adaptation could capture the salient features of the dynamic stall.

3.3 OA209 Finite Wing

To demonstrate the efficacy of the temporal error controller and mesh adaptive approaches, a three-dimensional finite wing has been evaluated. The aspect ratio three (3) wing is based on the OA209 airfoil and was evaluated in a wind tunnel using Particle Image Velocimetry (PIV), Laser Doppler Velocimetry (LDV), and unsteady Kulite pressure transducers for static and dynamic stall. The free stream velocity was $V_\infty = 55$ m/s corresponding to a $M_\infty = 0.16$ and a chord-based Reynolds number of $Re_c = 1 \times 10^6$. The tunnel blockage was determined to be minimal, with a measured tunnel turbulence of 0.05%. The dynamic stall tests were conducted with free transition for $\alpha = 17^\circ \pm 5^\circ \sin(\omega t)$ where $\omega = 3.5$ Hz or a reduced frequency, $k = 0.1$. Further details and data from the experimental campaign can be found in Le Pape et al.^[11].

The near-body grids extended to the farfield and did not utilize the off-body grid capabilities in OVER-

FLOW; therefore, only the near-body grid adaption option in OVERFLOW was applied. The non-adapted meshes were first assessed for static conditions to ensure that they were sufficient to capture the three-dimensionality of the finite wing. The final unadapted mesh size was approximately 26.5 million mesh points. A coarsened mesh of 16 million grid points was applied as the baseline for adaptation.

The mesh adaptation feature sensor was the undivided difference of the flow field conserved variables (Eq. 4). To control the grid growth, a growth ratio of 1.2 was applied with a total of two adaption levels. Error tolerances were adjusted using Newton's method to meet the grid constraints. In addition, smoothing of the error sensor function was applied to minimize disparate growth in adjacent regions, as well as weighting of the function that applied a decay away from the airfoil to minimize refinement in wake areas that would not impact the integrated performance quantities. The mesh was adapted at every 5 steps with a total of 18,000 time steps/cycle (3,600 adaptations). Only a third-order convergence during the Newton subiterations was achieved, unlike the fourth-order convergence observed for the two-dimensional simulations. The standard Spalart-Allmaras turbulence model was applied.

The mesh adaptation over the final (third) cycle is shown in Fig. 11. The upstroke mesh stayed relatively constant in size to the baseline mesh until the nonlinear lift region and the onset of dynamic stall was reached. At that time, the mesh size increased by approximately two million mesh points until reattachment near the beginning of the cycle. An example of how the near-body mesh adaption occurs dynamically can be observed in Fig. 12. The mesh, and accompanying snapshot of the near-body shed wake vorticity, for 13.42° on the upstroke and 20.53° on the downstroke illustrate the changing mesh. For the upstroke, the mesh remains relatively coarse, except for some refinement near the root. During the downstroke, where there is significant vorticity shed from the wing, there are multiple regions of mesh refinement that extend the entire wing span, with secondary refinement levels closer to the surface.

The lift and pitching moments are compared in Figs. 13 and Fig. 14, respectively with experimental data^[11]. The upstroke portion of the simulation for both the fixed grid and the adapted mesh are virtually identical for both lift and pitching moment. The primary differences between the two simulations occur during the onset of dynamic stall, recovering near the reattachment of the dynamic stall. The discrepancies between the two simulations is observed at all span stations, but the longest range of mismatching results occurs at the 50% ($r/R = 0.5$) span station. The adapted grid simulation does not recover the accuracy of the fixed grid simulation until $\alpha = 14^\circ$. The

abrupt reattachment observed at the inboard station is mitigated by the influence of the tip vortex in stations further outboard, as observed by the more gentle reattachment during the downstroke. The fixed and adapted grid results are comparable as early as $\alpha = 16^\circ - 18^\circ$, though the magnitude of the mismatches at higher angles of attack is larger than observed at the 50% span station. The increased lift that occurs in the experiment at the onset of the dynamic stall at the outboard stations is captured, albeit less intensely, by the adaptive grid but not by the fixed, refined grid. The magnitude of the maximum negative pitching moment is more accurately predicted by the adaptive mesh at the 50% span station, but is less accurate for the three outboard stations.

The cost of the simulation using the adaptive grid was approximately 50% of the cost of the simulation with the fixed, refined mesh. Further optimization of the number of refinement levels and growth factors are warranted to more accurately predict the separated region just after the onset of dynamic stall. The complex wake region may require more rapid cell growth and additional levels, while it is apparent that upstroke region will not benefit from further refinement. The vorticity flux or a similar parameter such as Q-criterion may identify regions where additional levels of refinement may be needed to maintain accuracy.

4 CONCLUSION

The ability to predict dynamic stall accurately is limited, based on the fixed temporal and spatial requirements of most state-of-the-art CFD solvers. A study has been performed to investigate the ability of temporal error controllers and feature-based mesh adaptation to mitigate these costs. In addition, an adaptive time step approach is proposed to further reduce the costs of these dynamic stall simulations in two and three dimensions. Based on the study performed on three different airfoil geometries in two and three dimensions, the following conclusions can be observed:

1. Temporal error controllers can be applied to maintain accuracy during the attached portion of the dynamic stall without the need to apply the maximum number of Newton subiterations at each time step.
2. During the separated portion of the dynamic stall only 2-3 orders of magnitude convergence were observed, while during the attached flow region, close to six orders of magnitude convergence can be obtained. Two orders of magnitude convergence is insufficient for accuracy without many physical time steps per cycle. Four orders of magnitude convergence are recommended as

it provides comparable accuracy for the three time step sizes examined.

3. Additional cost reduction (25%) can be obtained by increasing the physical time step without increasing the number of Newton subiterations during the upstroke (attached flow) portion of dynamic stall. A simple adaptive time step based on the direction of the pitch has been demonstrated.
4. A 50% reduction in time was demonstrated with two- and three-dimensional feature-based spatial adaptation. A two-level refinement with a growth rate of 1.2 was sufficient to capture the upstroke and recovery/reattachment of the dynamic stall. Additional refinement is warranted to more accurately capture the complex wake during dynamic stall onset and largely separately flow field following.

Simultaneous temporal and spatially adapting meshes have been demonstrated, resulting in cost savings of 50% to 70% from traditional fixed meshes and time step/Newton subiteration schemes. Additional development and optimization of these approaches for full rotors and advanced turbulence closures such as hybrid RANS-LES methods are underway.

ACKNOWLEDGEMENTS

The authors would like to gratefully acknowledge Onera, in particular Arnaud le Pape and Blanche Demaret, for providing the OA209 configuration and experimental data, as well as insights and suggestions in using the same. The OA209 simulations presented here are part of the United States/French International Partnership Agreement, Task 3 Dynamic Stall.

The authors would like to thank John Kearney and Ari Glezer of Georgia Tech for the VR7 experimental data.

The GIT investigations were supported by the U.S. Army/Navy/NASA Vertical Lift Research Center of Excellence with Mahendra Bhagwat serving as Program Manager and Technical Agent, grant number W911W6-11-2-0010 and Army Research Office project under grant number W911NF-13-1-0244, Technical Monitor Matthew Munson. Computational time was provided through the Department of Defense (DoD) High Performance Computing Modernization Program (HPCMP) from the DoD HPC Center ERDC DSRC on the Cray XE6.

The U.S. Government is authorized to reproduce and distribute reprints notwithstanding any copyright notation thereon. The views and conclusions contained in this document are those of the authors and should not be interpreted as representing the official policies, either expressed or implied, of the U.S. Government.

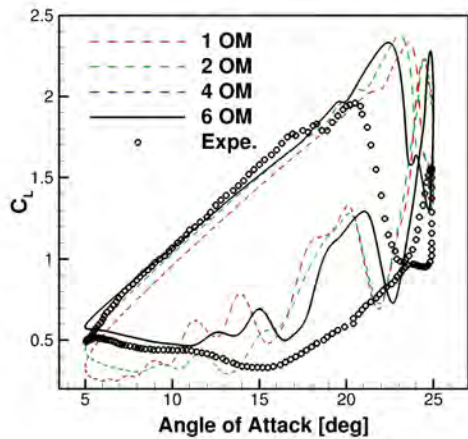
COPYRIGHT STATEMENT

The authors confirm that they, and/or their company or organization, hold copyright on all of the original material included in this paper. The authors also confirm that they have obtained permission, from the copyright holder of any third party material included in this paper, to publish it as part of their paper. The authors confirm that they give permission, or have obtained permission from the copyright holder of this paper, for the publication and distribution of this paper as part of the ERF2015 proceedings or as individual offprints from the proceedings and for inclusion in a freely accessible web-based repository.

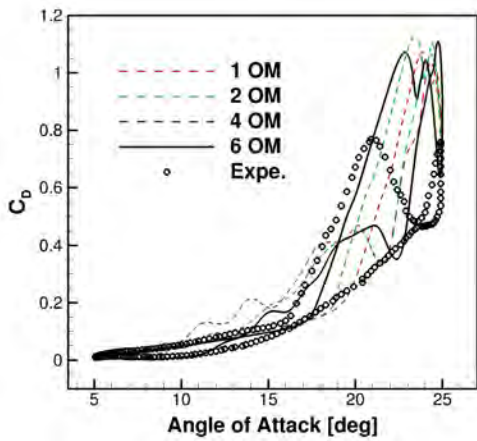
REFERENCES

- [1] Bousman, W. G., "A Qualitative Examination of Dynamic Stall from Flight Test Data," *Journal of the American Helicopter Society*, Vol. 43, (4), 1998, pp. 279–295.
- [2] McCroskey, W., "The Phenomenon of Dynamic Stall," Technical report, NASA TM-81264, 1981.
- [3] McCroskey, W. and Fisher, K., "Detailed Aerodynamic Measurements on a Model Rotor in the Blade Stall Regime," *Journal of the American Helicopter Society*, Vol. 17, (1), 1972, pp. 20 – 30.
- [4] Chandrasekhara, M. S., Wilder, M. C., and Carr, L. W., "Compressible Dynamic Stall Control: Comparison of Two Approaches," *Journal of Aircraft*, Vol. 38, (3), 2001, pp. 448–453.
- [5] Lorber, P. F., Covino, A. F. J., and Carta, F. O., "Dynamic Stall Experiments on a Swept Three-Dimensional Wing in Compressible Flow," AIAA 91-1795-CP, 22nd Fluid Dynamics, Plasma Dynamics & Lasers Conference, Honolulu, Hawaii, June 1991.
- [6] Lorber, P. and Carta, F., "Airfoil Dynamic Stall at Constant Pitch Rate and High Reynolds Number," *Journal of Aircraft*, Vol. 25, (6), 1988, pp. 548–556.
- [7] Piziali, R., Aeronautics, N., and Space Administration. Ames Research Center, C., Moffett Field, "2-D and 3-D Oscillating Wing Aerodynamics for a Range of Angles of Attack Including Stall," Technical report, National Aeronautics and Space Administration. Ames Research Center, Moffett Field, CA., 1994.
- [8] Hodara, J., Lind, A., Jones, A., and Smith, M., "Collaborative Investigation of the Aerodynamic Behavior of Airfoils in Reverse Flow (AHS Paper 2015-267)," American Helicopter Society 71st Annual Forum, May 2015.
- [9] Kearney, J. M., *Aerodynamic Control Using Distributed Active Bleed*, Ph.D. thesis, Georgia Institute of Technology, Atlanta, GA, 2015.

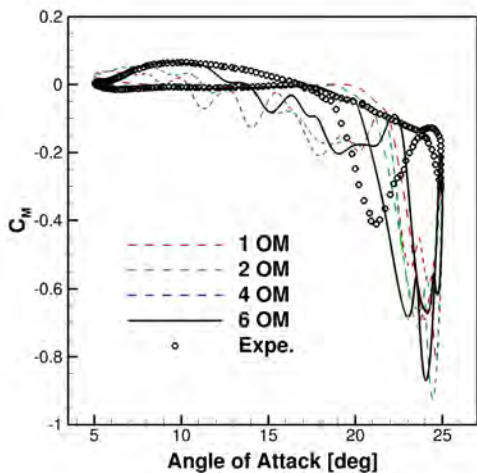
- [10] Datta, A., Yeo, H., and Norman, R., "Experimental Investigation and Fundamental Understanding of a Full-Scale Slowed Rotor at High Advance Ratios," *Journal of the American Helicopter Society*, Vol. 58, (2), 2013, pp. 1–17.
- [11] Le Pape, A., Pailhas, G., David, F., and Deluc, J.-M., "Extensive Wind Tunnel Tests Measurements of Dynamic Stall Phenomenon for the OA209 Airfoil Including 3D Effects," 33rd European Rotorcraft Forum, Kazan, Russia, 11–13 September 2007.
- [12] Szydowski, J. and Costes, M., "Simulation of Flow Around a Static and Oscillating in Pitch NACA0015 Airfoil using URANS and DES," Proceedings of the ASME Heat Transfer/Fluids Engineering Summer Conference, Charlotte, NC, July 11–15 2004.
- [13] Gleize, V., Szydowski, J., and Costes, M., "Numerical and Physical Analysis of the Turbulent Viscous Flow Around a NACA0015 Profile at Stall," European Congress on Computational Methods in Applied Sciences and Engineering, July 24–28, 2004.
- [14] Costes, M., Gleize, V., and Szydowski, J., "Grid Sensitivity Study for the Turbulent Viscous Flow Around a NACA0015 Airfoil at Stall," 31st European Rotorcraft Forum, Florence, Italy, September 13–15 2005.
- [15] Costes, M., Gleize, V., Le Pape, A., and Richez, F., "Numerical Investigation of Laminar/Turbulent Transition Effects on the Dynamic Stall of an Oscillating Airfoil," AHS Specialists Conference on Aerodynamics, San Francisco, CA, January 23–25 2008.
- [16] Klein, A., Richter, K., Altmikus, A., Lutz, T., and Kramer, E., "Unsteady Criteria for Rotor Blade Airfoil Design," 35th European Rotorcraft Forum, September 22–25, 2009.
- [17] Richter, K., Le Pape, A., Knopp, T., Costes, M., Gleize, V., and Gardner, A., "Improved Two-Dimensional Dynamic Stall Prediction with Structured and Hybrid Numerical Methods," *Journal of the American Helicopter Society*, Vol. 56, (4), 2011, pp. 042007(1–12).
- [18] Liggett, N. and Smith, M. J., "Temporal Convergence Criteria for Time-Accurate Viscous Simulations of Separated Flows," *Computers & Fluids*, Vol. 66, 2012, pp. 140–156.
doi: 10.1016/j.compfluid.2012.06.010
- [19] Burgess, N. and Jain, R., "Effects of Numerical Methods on Static and Dynamic Stall Simulations," AHS Aeromechanics Specialists Conference, San Francisco, CA, January 2012.
- [20] Kaufmann, K., Costes, M., Richez, F., Gardner, A. D., and Le Pape, A., "Numerical Investigation of Three-Dimensional Static and Dynamic Stall on a Finite Wing," *Journal of the American Helicopter Society*, Vol. 60, (3), 2015, pp. 1–12.
- [21] Smith, M. J., Liggett, N., and Koukol, B. C. G., "The Aerodynamics of Airfoils at High and Reverse Angles of Attack," *AIAA Journal of Aircraft*, Vol. 48, (6), 2011, pp. 2012–2023.
doi: 10.2514/1.55358
- [22] Moulton, M., Smith, M. J., Wong, T.-C., Le Pape, A., and Le Balleur, J.-C., "The Role of Transition Modeling in CFD Predictions of Static and Dynamic Stall," 37th European Rotorcraft Forum, Sept. 2011.
- [23] Jespersen, D., Pulliam, T., and Buning, P., "Recent Enhancements to OVERFLOW," AIAA Paper 97-0644, 35th Aerospace Sciences Meeting, Reno, NV, 6–9 Jan., 1997.
- [24] Biedron, R. T., Vatsa, V. N., and Atkins, H. L., "Simulation of Unsteady Flows Using an Unstructured Navier-Stokes Solver on Moving and Stationary Grids," *AIAA paper*, Vol. 5093, 2005, pp. 2005.
- [25] Nichols, R. H., Tramel, R. W., and Buning, P., "Solver and Turbulence Model Upgrades to OVERFLOW 2 for Unsteady and High-Speed Applications," AIAA 2006-2824, 25th Applied Aerodynamics Conference, 5–8 June 2006.
- [26] Vatsa, V. N. and Carpenter, M. H., "Higher Order Temporal Schemes with Error Controllers for Unsteady Navier-Stokes Equations," AIAA 2005-5245, 17th AIAA Computational Fluid Dynamics Conference, Toronto, CA, 6–9 June, 2005.
- [27] Menter, F. R., Kuntz, M., and Langtry, R., "Ten Years of Industrial Experience with the SST Turbulence Model," *Turbulence, Heat and Mass Transfer*, Vol. 4, 2003, pp. 625–632.
- [28] Buning, P. G. and Pulliam, T. G., "Recent Enhancements to OVERFLOW for Spatial and Temporal Adaption," 12th Symposium on Overset Composite Grid and Solution Technology, Atlanta, GA, 6–9 October 2014.



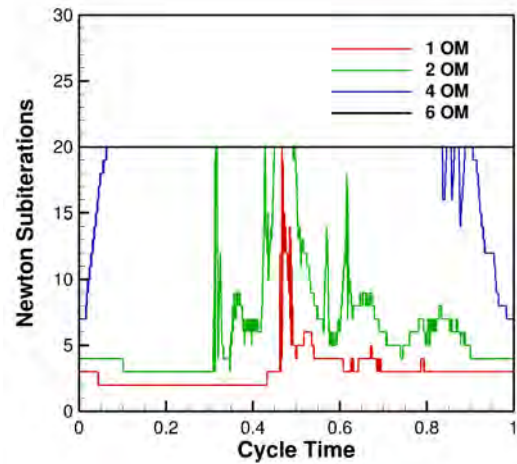
(a) Lift coefficient



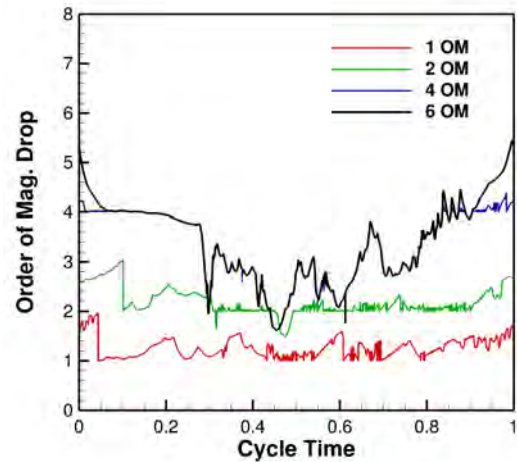
(b) Drag coefficient



(c) Pitching moment coefficient



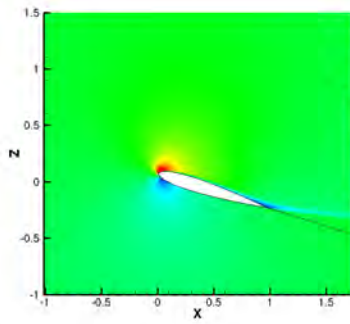
(a) Newton Subiterations - 9,000 steps



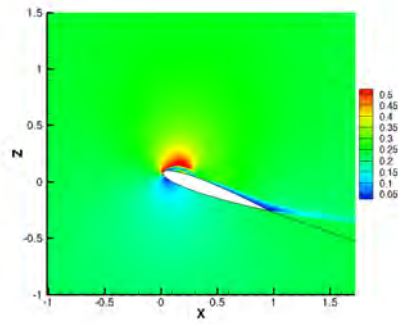
(b) Order of Mag. Drop - 9,000 steps

Fig. 2: Number of Newton subiterations required to reach the specified order of magnitude drop in the residuals.

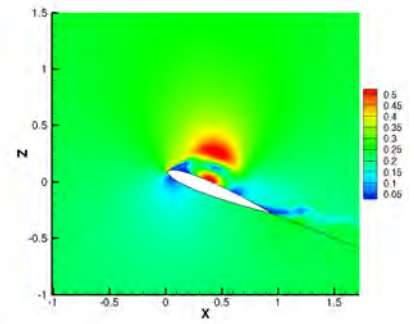
Fig. 1: Two-dimensional OVERFLOW computational analyses using the Menter SST model for an NACA0012 airfoil undergoing dynamic stall with temporal error controllers. A time step of 9,000 time steps per cycle and 40 Newton subiterations was applied.



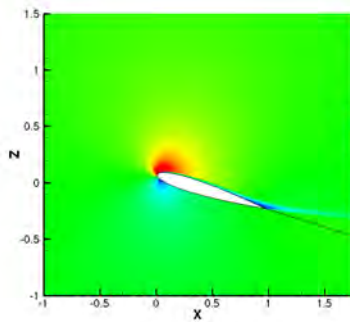
(a) $\alpha = 17.42^\circ - 1OM$



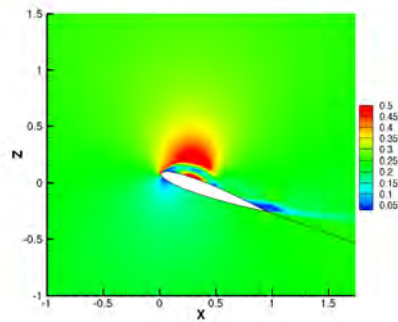
(b) $\alpha = 19.76^\circ - 1OM$



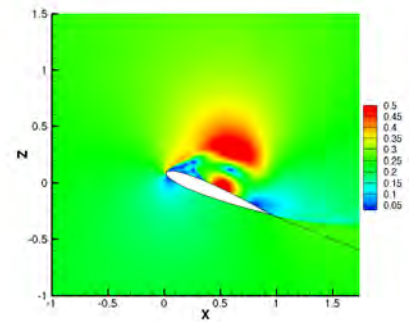
(c) $\alpha = 21.79^\circ - 1OM$



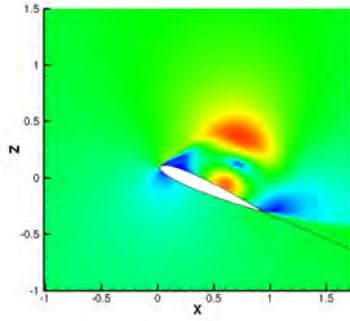
(d) $\alpha = 17.42^\circ - 4OM$



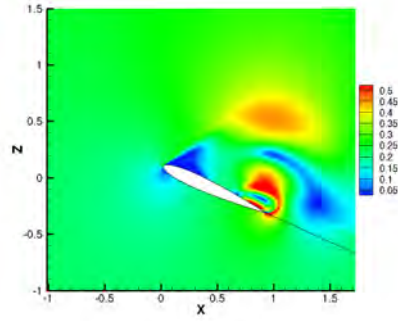
(e) $\alpha = 19.76^\circ - 4OM$



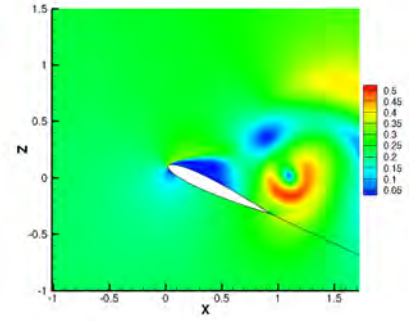
(f) $\alpha = 21.79^\circ - 4OM$



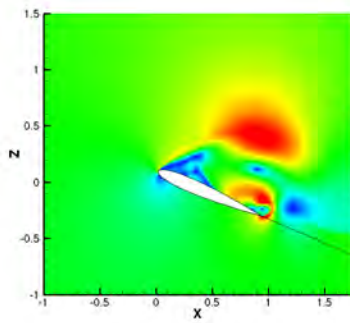
(g) $\alpha = 23.41^\circ - 1OM$



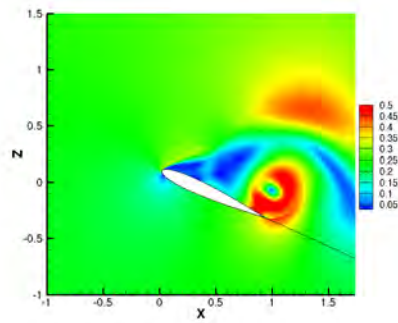
(h) $\alpha = 24.49^\circ - 1OM$



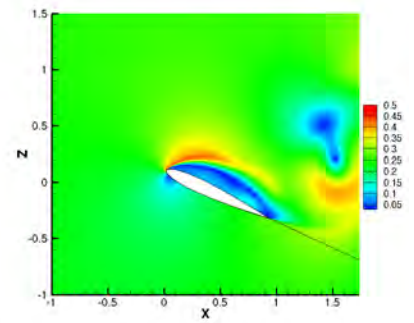
(i) $\alpha = 24.98^\circ - 1OM$



(j) $\alpha = 23.41^\circ - 4OM$

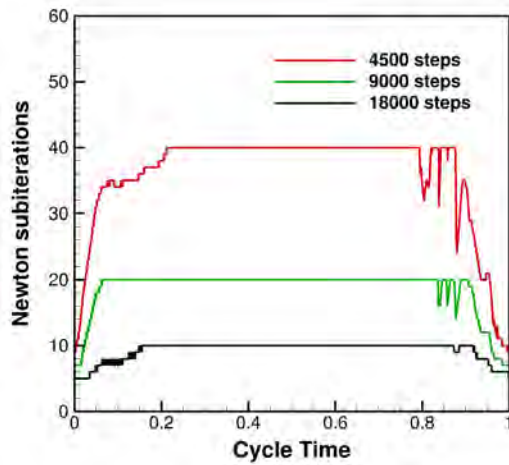


(k) $\alpha = 24.49^\circ - 4OM$

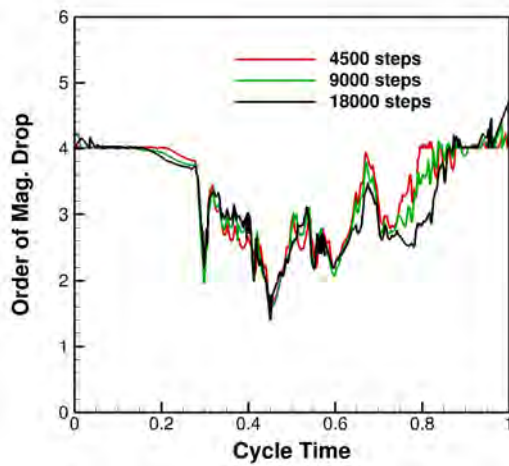


(l) $\alpha = 24.98^\circ - 4OM$

Fig. 3: Impact of number of order of magnitude drop on the flow field.

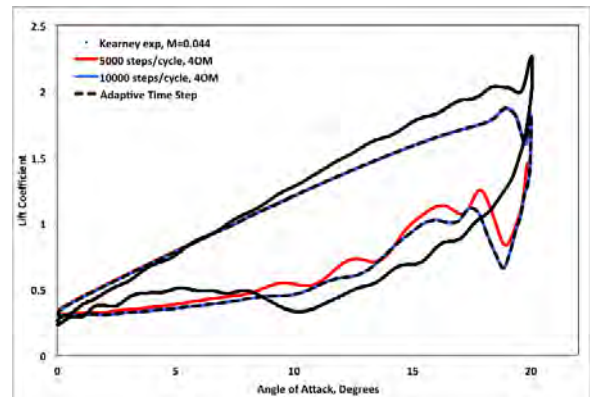


(a) Newton Subiterations - 4OM

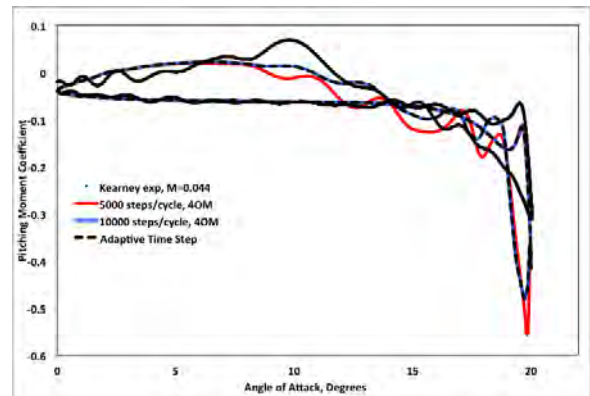


(b) Order of Mag. Drop - 4OM

Fig. 4: Number of Newton subiterations required to reach the specified order of magnitude drop in the residuals.

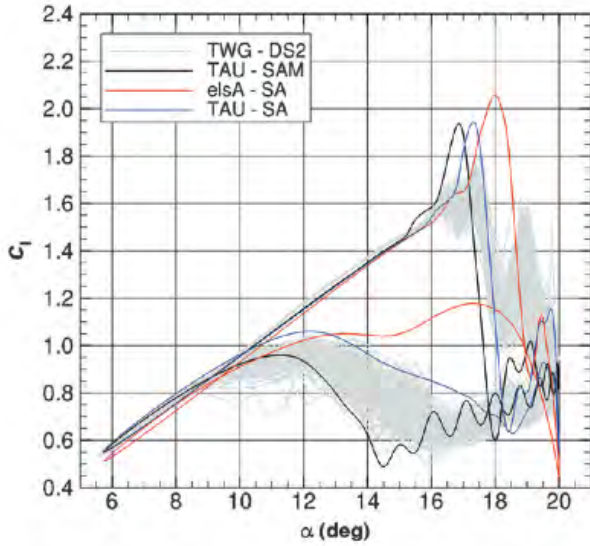


(a) Lift coefficient

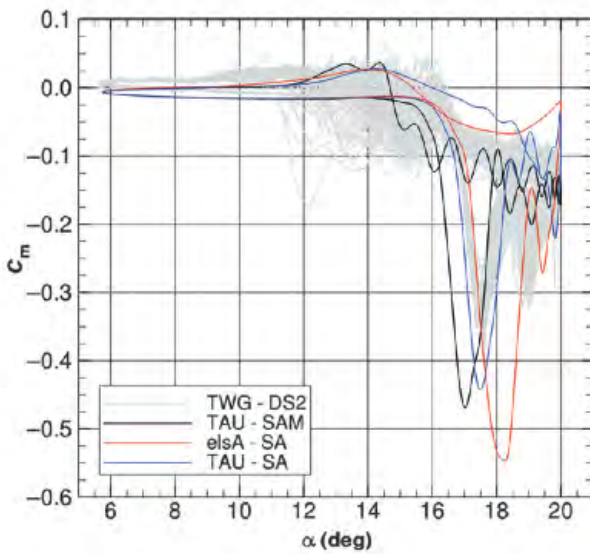


(b) Pitching moment coefficient

Fig. 5: Time adaptation during dynamic stall for a VR7 (no tab) airfoil undergoing dynamic stall at $k = 0.13$.



(a) Lift coefficient



(b) Pitching moment coefficient

Fig. 6: Two-dimensional computational analyses using the Spalart-Allmaras model for an OA209 airfoil undergoing deep dynamic stall. From Richter et al. [17].

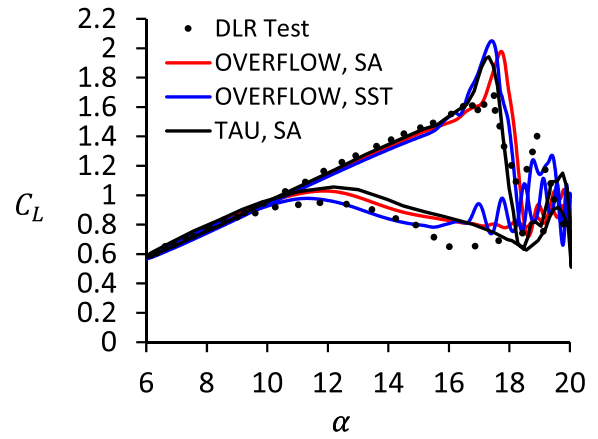
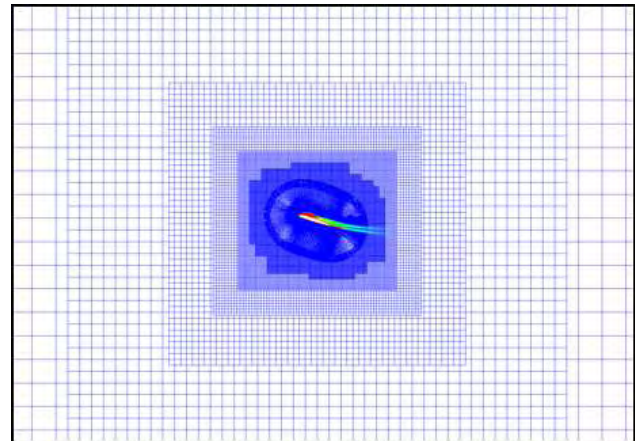
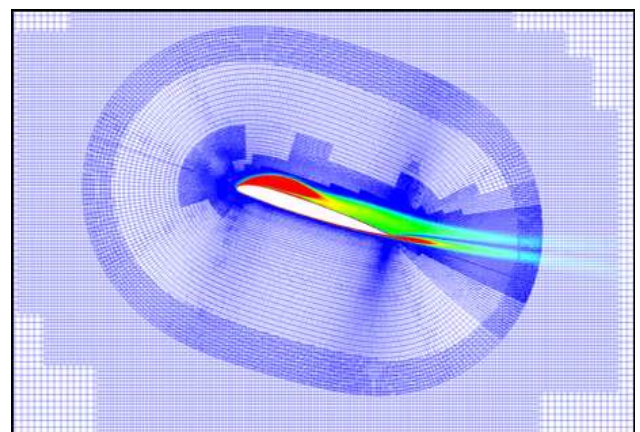


Fig. 7: Demonstration that OVERFLOW without adaptation obtains similar results to Richter et al. [17].



(a) Full mesh



(b) Airfoil mesh with adaptation

Fig. 8: OVERFLOW airfoil mesh for the OA209 airfoil with near-body mesh adaptation.

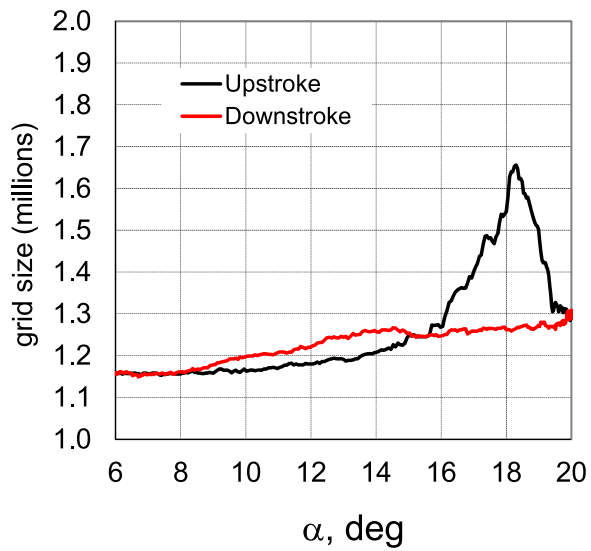
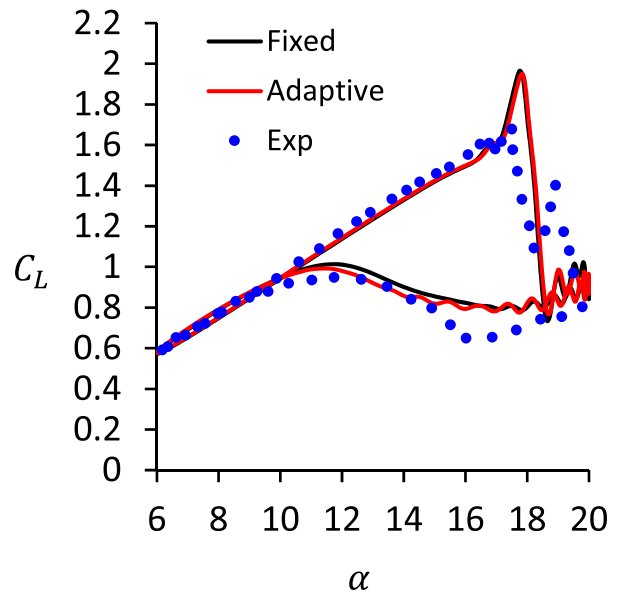
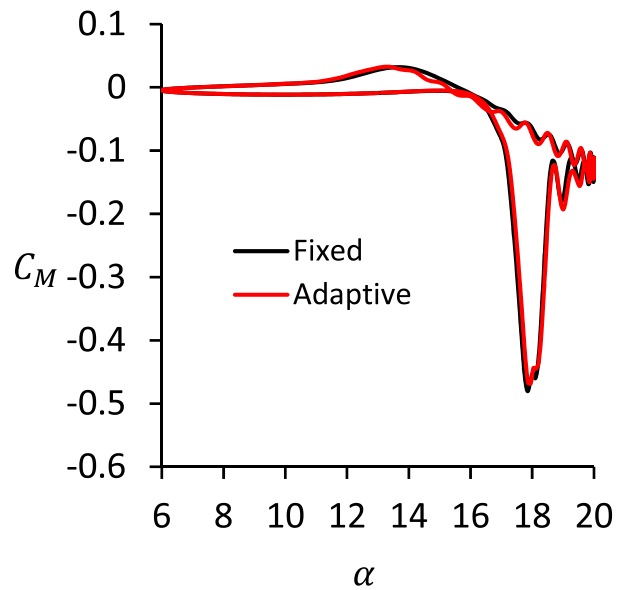


Fig. 9: Mesh adaptation for the OA209 airfoil undergoing deep dynamic stall.



(a) Lift coefficient



(b) Pitching moment coefficient

Fig. 10: Two-dimensional OVERFLOW computational analyses using the Spalart-Allmaras model for an OA209 airfoil undergoing deep dynamic stall with and without mesh refinement.

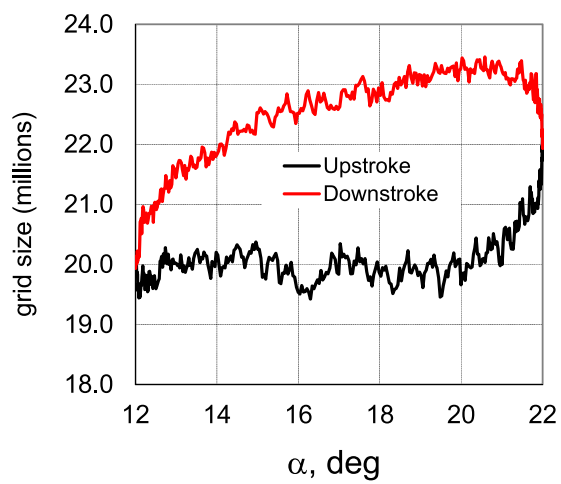
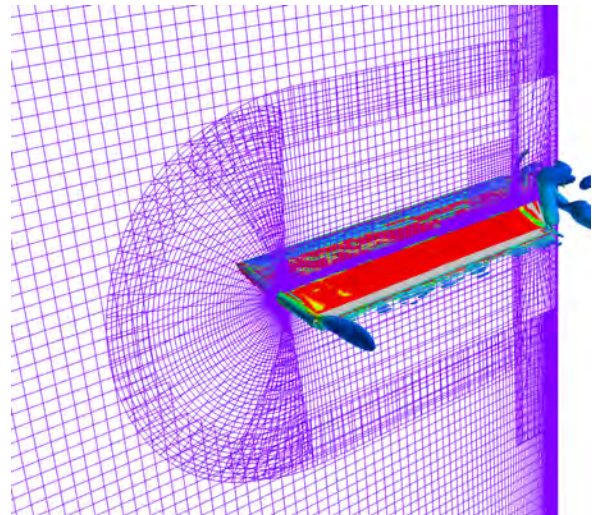
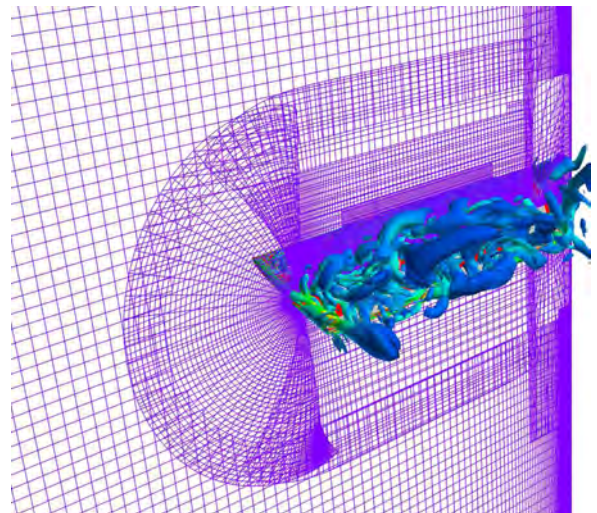


Fig. 11: Mesh adaptation for the three-dimensional OA209 finite wing undergoing dynamic stall.

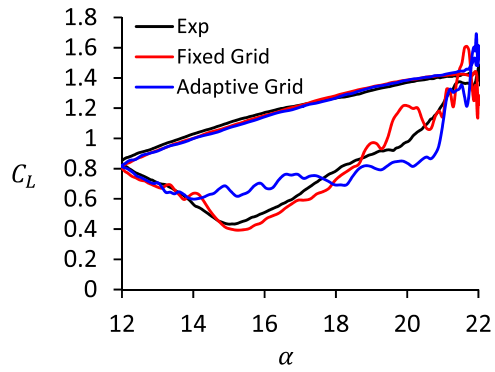


(a) 13.42° upstroke

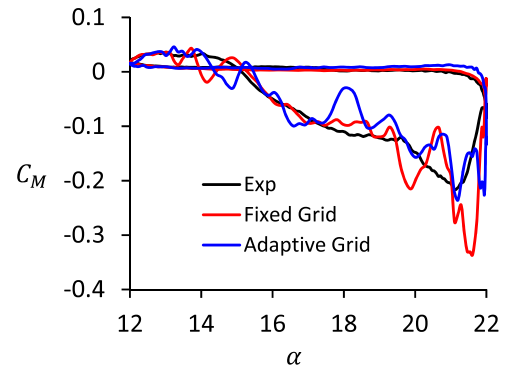


(b) 20.53° downstroke

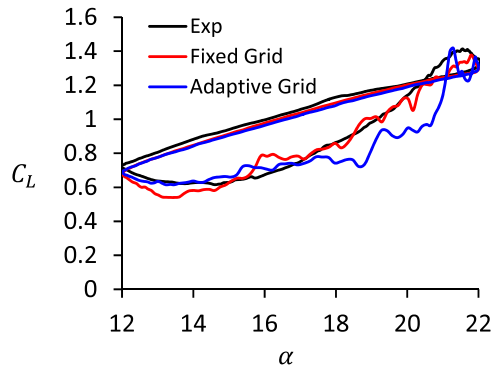
Fig. 12: Dynamic mesh adaptation and near-body shed wake for the OA209 finite wing during dynamic stall



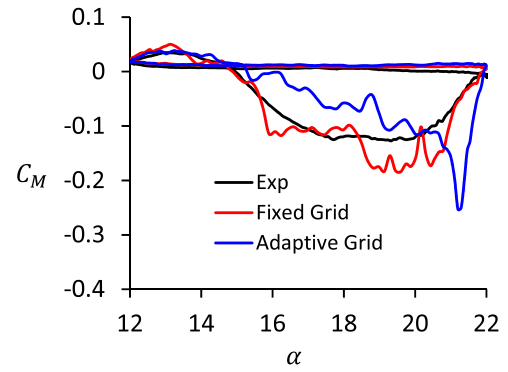
(a) $r/R = 0.5$



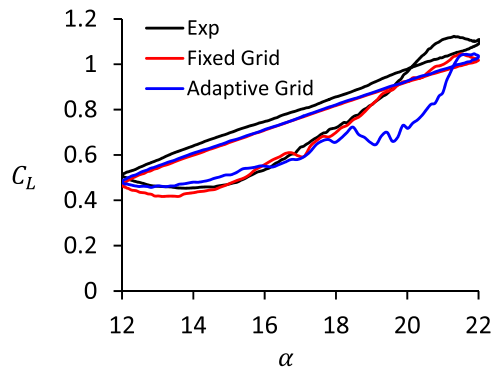
(a) $r/R = 0.5$



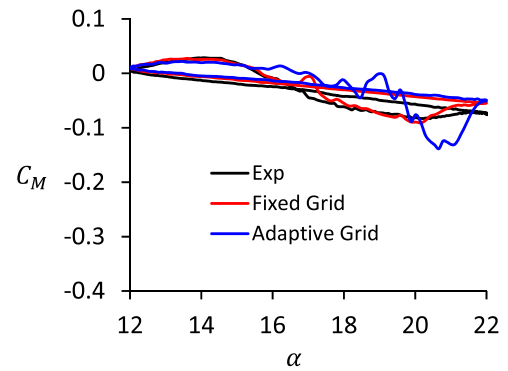
(b) $r/R = 0.8$



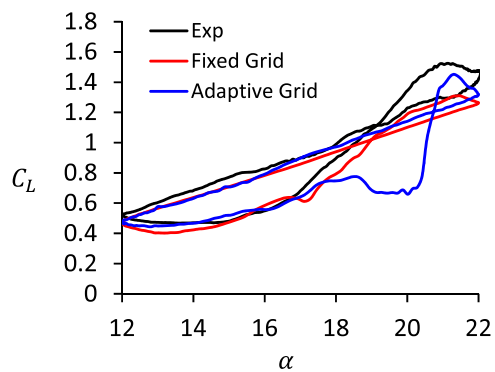
(b) $r/R = 0.8$



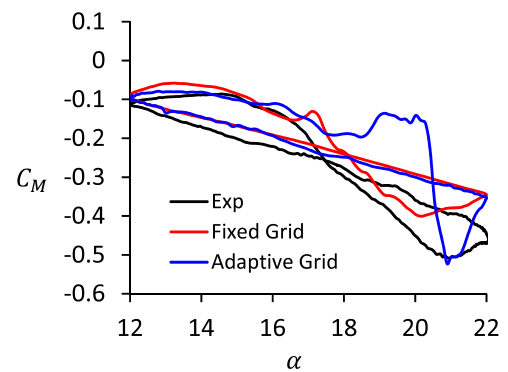
(c) $r/R = 0.95$



(c) $r/R = 0.95$



(d) $r/R = 0.99$



(d) $r/R = 0.99$

Fig. 13: Lift coefficient comparison of the refined mesh, adapted mesh, and experiment^[11].

Fig. 14: Pitching moment coefficient comparison of the refined mesh, adapted mesh, and experiment^[11].